ChemPubSoc Europe

DOI: 10.1002/cphc.201701266

CHEMPHYSCHEM Articles

Towards the Detection of Explosive Taggants: Microwave and Millimetre-Wave Gas-Phase Spectroscopies of 3-Nitrotoluene

Anthony Roucou,*[a] Isabelle Kleiner,[b] Manuel Goubet,[c] Sabath Bteich,[c] Gael Mouret,[a] Robin Bocquet,[a] Francis Hindle,[a] W. Leo Meerts,[d] and Arnaud Cuisset*[a]

The monitoring of gas-phase mononitrotoluenes is crucial for defence, civil security and environmental interests because they are used as taggant for TNT detection and in the manufacturing of industrial compounds such as dyestuffs. In this study, we have succeeded to measure and analyse at high-resolution a room temperature rotationally resolved millimetre-wave spectrum of *meta*-nitrotoluene (3-NT). Experimental and theoretical difficulties have been overcome, in particular, those related to the low vapour pressure of 3-NT and to the presence of a CH_3 internal rotation in an almost free rotation regime ($V_3 = 6.7659(24)$ cm^{-1}). Rotational spectra have been recorded in the microwave and millimetre-wave ranges using a supersonic jet Fourier Transform microwave spectrometer ($T_{rot} <$ 10 K) and a millimetre-wave frequency multiplication chain ($T = 293$ K), respectively. Spectral analysis of pure rotation lines in the vibrational ground state and in the first torsional excited state supported by quantum chemistry calculations permits the rotational energy of the molecule, the hyperfine structure due to the ^{14}N nucleus, and the internal rotation of the methyl group to be characterised. A line list is provided for future in situ detection.

1. Introduction

In recent years, intensive research has failed to develop a compact and low-cost explosive vapour sensor with a part per billion limit of detection capable of replacing the trained canine. Although high-resolution rovibrational spectroscopy has proven to be a powerful tool for the detection, identification and quantification of gas-phase molecular species of atmospheric and astrophysical interest, the optical methods employed have encountered the problem of room temperature detection of weakly volatile explosive vapours due to a lack of sensitivity. Indeed, energetic compounds have very low vapour pressures at room temperature. For example, TNT is one of the most volatile energetic materials, with a vapour pressure of 1.3 mPa at 300 K.[1] Vapour pressures of most of the other energetic materials such as cyclo-1,3,5-trimethylene-2,4,6-trinitramine (RDX) and pentaerythritol tetranitrate (PETN) are significantly lower by several orders of magnitude. On the basis of this observation, the gas-phase spectroscopic measurement of explosives requires a shift towards the most sensitive methods of detection

In 2004, D. S. Moore published a review dealing with instrumentation for trace detection of explosives.[2] Several spectroscopic techniques were considered, but each of them presents some specific disadvantages for the unambiguous detection of the explosive vapour: ultrasensitive photothermal deflection,[3] cavity-ringdown[4] and photoacoustic[5] IR methods, probing intense vibrational transitions, could be used to measure the gas-phase signatures of TNT and RDX classical explosives at a sub-ppm level but do not allow the unambiguous discrimination of compounds of the same family and isomers; Raman spectroscopy has been used to detect residual explosives in fingerprint samples[6] but its ability to detect very small solid samples failed in the gas phase because of a lack of sensitivity; finally, promising results on TNT detection have been obtained in the UV/Visible domain by laser photofragmentation[7] or single photon ionisation[8] but these methods did not exclude the possibility of the parent molecule fragmentation.

To somewhat alleviate the low-vapour-pressure problem for the detection of explosives, various taggants are used in many commercially manufactured explosives.[9] Isomers of mononi-

[a] *A. Roucou, Prof. G. Mouret, Prof. R. Bocquet, Dr. F. Hindle, Dr. A. Cuisset*
Laboratoire de Physico-Chimie de l'Atmosphère (LPCA)
EA 4493, Université du Littoral Côte d'Opale
Maison de la Recherche en Environnement Industriel 2 (MREI2)
189A, Avenue Maurice Schumann
59140 Dunkerque (France)
E-mail: anthony.roucou@univ-littoral.fr
arnaud.cuisset@univ-littoral.fr

[b] *Prof. I. Kleiner*
Laboratoire Interuniversitaire des Systèmes Atmosphériques (LISA)
CNRS UMR 7583, Universités Paris-Est Créteil & Paris Diderot
61 avenue du Général de Gaulle
F-94010 Créteil cedex (France)

[c] *Dr. M. Goubet, S. Bteich*
Université Lille 1, CNRS
UMR8523-PhLAM-Physique des Lasers Atomes et Molécules
F-59000 Lille (France)

[d] *Prof. W. L. Meerts*
Radboud University, Institute for Molecules and Materials
Felix Laboratory, Toernooiveld 7c
6525 ED Nijmegen (The Netherlands)

Supporting Information and the ORCID identification number(s) for the author(s) of this article can be found under: https://doi.org/10.1002/cphc.201701266.

trotoluene are used as taggant for TNT detection (3-nitrotoluene (3-NT), 0.5%; or 2-nitrotoluene (2-NT), 0.5%). In addition to the defence and civil security interests, monitoring of nitrotoluene compounds is also relevant in industrial environmental topics because they are widely used in the manufacturing of dyestuffs, rubbers, pesticides and drugs,[10] and they are persistent in natural conditions. With a room temperature vapour pressure of about 10 Pa,[11] 10^4 times higher than that of TNT, the gas-phase detection of mononitrotoluenes at trace levels with usual spectroscopic techniques is possible and some new spectral windows at larger wavelengths may be used. For these reasons, studies of new spectroscopic rotational and vibrational signatures of nitro-derivative vapours in the THz domain have been undertaken.

At room temperature, far-infrared (FIR) vibrational gas-phase cross-sections of the three isomeric forms of NT have been measured and assigned at low resolution ($\Delta\nu = 0.5\ cm^{-1}$).[12] The results highlight the selectivity of gas-phase THz/FIR spectroscopy allowing an unambiguous identification of nitroaromatic compounds. In this study, rotational patterns have been observed and simulated but it was not possible to resolve the rotational structure of the rovibrational FIR bands. Despite the highest available resolution of the FTIR instrument ($10^{-3}\ cm^{-1}$), the density of rovibrational lines is so great that it prevented their individual observation at room temperature. This is probably due to the low value of the rotational constants, hot bands and splitting due to large amplitude motions. Considering that the resolution of the rovibrational structure of FIR fundamental bands at very low temperature is out of reach,[13] the opportunity to probe pure rotational transitions of explosive taggants in the microwave (MW) and millimetre (mm) wavelength ranges using electronic sources with exceptional spectral purities has been considered. By targeting mononitrotoluene isomers, experimental and theoretical difficulties should be overcome. From an experimental point of view, high-performance instrumentation is required to ensure the sensitivity and selectivity for these molecules. Indeed, high sensitivity is needed to measure weak signals with sufficient signal-to-noise ratio (S/N) at room temperature and high-resolution measurements are essential to resolve the heavily congested spectra.

Concerning the spectroscopic analysis, a specific effective Hamiltonian taking into account large amplitude motion and hyperfine structure was required. Especially, the internal rotation of the methyl group, depending on the barrier height and therefore on the isomeric form, has to be specifically treated. According to this, although rotational spectra of nitrobenzene compounds have been measured and analysed in the early 70s,[14] no high-resolution rotational studies have been carried out on nitrotoluenes. To date, a limited number of systems containing both almost free internal rotors and a nitrogen atom (quadrupolar nucleus) have been studied by rotational spectroscopy.[15,16]

To our knowledge, the only attempt to resolve rotationally the gas-phase spectra of an explosive taggant was performed in 2006, by Foltynowicz et al.,[17] using medium-resolution THz-Time Domain Spectroscopy. This study emphasises the difficulty to measure the gas-phase rotational spectrum of an explosive derivative such as 2,4-dinitrotoluene (2,4-DNT). Indeed, the best results were obtained with a static pressure lower than 0.005 Pa at 150 °C for 4 hours. Only the pure rotation pattern of the 2,4-DNT vapour was observed below 0.5 THz with a relatively poor S/N (<3). No assignment of individual rotational transitions was performed because of the insufficient resolution and sensitivity. In this study, we present the first high-resolution gas-phase analysis of an explosive taggant of TNT: 3-NT. The geometry of the molecule, in the Principal axis orientation (PAM), optimised at the MP2/cc-VQZ level of theory is presented in Figure 1. 3-NT is a prolate asymmetric top ($\kappa = -0.75$) belonging to the G_6 Permutation Inversion group (a C_s frame and a C_{3v} top for the methyl group)[18] with a strong permanent dipole moment ($\mu \approx 5.4$D) in the (a,b) plane (cf. Figure 1).

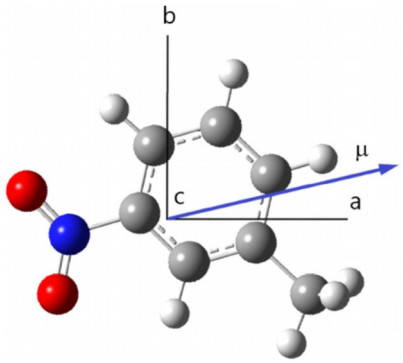

Figure 1. Geometry of the 3-nitrotoluene in the principal axis orientation optimised at the MP2/cc-pVQZ level of theory.

With the support of high level electronic structure calculations, the jet-cooled MW spectrum was first measured and fitted using the BELGI-C_s-hyperfine code, providing a set of ground-state molecular constants allowing the lowest energy levels (up to $J = 11$) to be determined, taking into account both the coupling between global rotation of 3-NT and the internal rotation of the methyl group as well as the nuclear quadrupole coupling (NQC) due to the ^{14}N atom. The obtained constants have then been used as initial parameters for analysis of the room-temperature mm-wave spectrum. A global fit has been performed allowing the MW and mm-wave transition frequencies in the vibrational ground state and in the first torsional excited state ($\nu_{t_{CH_3}} = 0$ and 1, respectively) to be reproduced at the experimental accuracies. NQC constants, internal rotation potential and limitations of the model are specifically discussed.

2. Results and Discussion

2.1. Jet-Cooled MW Spectrum Analysis

The jet-cooled pure rotation spectrum of 3-NT was measured in the 4–20 GHz frequency range using the supersonic jet Fabry–Pérot Fourier-transform microwave (FP-FTMW) spectrometers of the PhLAM Laboratory in Lille (see Section 4.1).[19,20] Two sets of $J'_{K'_a,K'_c} \rightarrow J''_{K''_a,K''_c}$ rotational transitions (a-

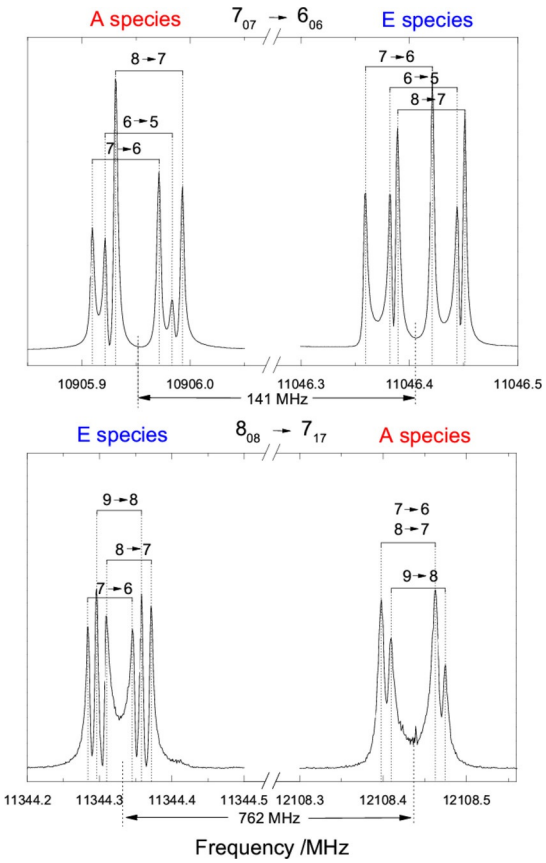

Figure 2. Experimental spectrum of [a]R-type ($7_{07} \rightarrow 6_{06}$, 50 co-added scans for A and E species) and [b]R-type ($8_{08} \rightarrow 7_{17}$, 300 and 1000 co-added scans for A and E species, respectively) MW transitions. The hyperfine structures due to the ^{14}N quadrupolar nucleus are clearly observed (assignments the format $F' \rightarrow F''$).

type and b-type) observed around 11 GHz are displayed in Figure 2. Each multiplet is composed of six signals (the Doppler doublet of the three most intense NQC components). The methyl group of 3-NT undergoes internal rotation and causes all rotational lines to split into A and E components.[21,22] The height of the internal rotation barrier (V_3) has been estimated as 6.6 cm^{-1} at the MP2/CBS (ZPE corrected) level of theory (see Section 4.3 for details). The internal rotation constant F has been estimated from MP2/cc-pVQZ calculations as 5.4 cm^{-1}, leading to a reduced barrier height $s = \frac{4V_3}{9F} = 0.36$. With such a very low value, huge A-E splittings (from hundreds of MHz up to several GHz) were expected in the FP-FTMW spectrum and the A-E doublets cannot be straightforwardly identified even in the ground torsional state $v_{t_{CH_3}} = 0$. It should be noted that in such a molecule with E levels above the barrier height, the free rotor quantum number m should be used instead of $v_{t_{CH_3}}$ as described by Ilyushin et al.[23,24] with the following connections: $v_{t_{CH_3}} = 0$ A$\rightarrow m = 0$, $v_{t_{CH_3}} = 0$ E$\rightarrow m = \pm 1$, $v_{t_{CH_3}} = 1$ A$\rightarrow m = +3$, $v_{t_{CH_3}} = 1$ E$\rightarrow m = \pm 2$. However, $v_{t_{CH_3}}$ is used by the model presently implemented in BELGI-C$_s$-hyperfin, so we decided to keep the use of this quantum number.

In an initial step, using the SPFIT/SPCAT Pickett's programs (Watson-type semi-rigid rotor model in the I^r representation of A reduction Hamiltonian),[25] the A components were assigned without taking into account the CH_3 internal rotation by performing an effective fit including, however, the ^{14}N NQC term. Concerning the rotational constants, the fitting process was started using "hybrid" values from quantum chemistry calculations and taking into account the internal rotation correction for the A components using D. R. Herschbach formalism [see Eqs. (6) and (7) in Section 4.3]. Electric dipole moment components and NQC constants calculated at the MP2/cc-pVQZ level of theory have also been used as starting values (see Table S1 with all the calculated parameters used as starting values for the fit).

The BELGI-C$_s$-hyperfine code was then used, which is a slightly modified version of the BELGI-C$_1$-hyperfine code allowing for treatment of internal rotation effects with hyperfine structure for molecules with a planar frame.[16,26] The code uses the "Rho-Axis-method" (RAM) to minimise the torsion-rotation coupling in an effective Hamiltonian.[27] Like in BELGI-C$_1$-hyperfine, the present code deals with the effect of the weak NQC using a perturbation approach similar to that used for acetamide,[15] a Cs molecule with one methyl internal rotor.[16]

As starting values for the fit using the BELGI-C$_s$-hyperfine code, we used the calculated "hybrid" rotational constants corrected for A and E species according D. R. Herschbach (see Table 1 and Equation (6) and (7) in Section 4.3) and the calculated dipole moment components in the RAM axis system obtained by a rotation of a and b axes of an angle $\theta_{RAM} = -19.318^\circ$ calculated from Eq. (9) (see Section 4.3). The NQC hyperfine parameters were taken from the SPFIT simulation and

Table 1. Rotational and torsion-rotation parameters for 3-NT from the BELGI-C$_s$-hyperfine code converted into the PAM system. The fitted parameters are compared to calculated values (see Section 4.3). All constants refer to the PAM system and statistical uncertainties are given in parentheses as one standard deviation in the last digits.

	Unit	BELGI-C$_s$-hyperfine	Calculated
A	MHz	2662.853(33)	2661.861[a]
B	MHz	982.0909(41)	991.031[a]
C	MHz	721.63029(35)	725.568[a]
V_3	cm^{-1}	6.7659(24)	6.63[b]
V_6	cm^{-1}	0.02333(22)	
ρ	unitless	0.01273920(48)	0.001267[c]
F	cm^{-1}	5.386202(82)	5.4584[c]
θ_{RAM}	deg	−19.18639(74)[d]	−19.318[c]
$\angle(i,a)$	deg	−43.3346(17)[e]	−43.248[c]
unitless standard deviation		MW:0.942[f]/mm-wave: 0.983[f]	

[a] Calculated rotational constants are $A_0^{corr.}$, $B_0^{corr.}$ and C_0^{hybrid}, see Section 4.3 for details. [b] Calculated internal rotation barrier V_3 at the MP2/CBS level ZPE corrected. [c] ρ [see Eq. (5)], F [see Eq. (5)], θ_{RAM} [see Eq. (9)] and $\angle(i,a)$ [see Eq. (10)], I_a, I_b and I_c are estimated from A_0^{hybrid}, B_0^{hybrid} and C_0^{hybrid} constants, and the direction cosines λ_g and I_α are estimated from the MP2/cc-pVQZ equilibrium structure. [d] The BELGI-C$_s$-hyperfine value of θ_{RAM} is defined as: $tan(2\theta_{RAM}) = \frac{2*D_{ab}}{B_{RAM} - A_{RAM}}$ with D_{ab} the "Coriolis-like" operator coefficient corresponding to the off-diagonal element of the inertial tensor in RAM system.[26] [e] The BELGI-C$_s$-hyperfine value of the angle $\angle(i,a)$ is obtained from Equation (10) using the fitted constants. [f] Unitless standard deviation of the fit defined as: $\sqrt{\frac{1}{N}\sum_i \left(\frac{f_i^{obs.} - f_i^{calc.}}{\Delta_i}\right)^2}$ with N the numbers of fitted lines and Δ_i the experimental accuracy.

also transformed into the RAM system. Internal rotation parameters V_3, F and ρ were estimated from the calculated molecular structure at equilibrium (see Section 4.2 and Table S1 with all the calculated parameters used as starting values for the fit). As an intermediate fit including only the microwave data, we used the three rotational constants A, B, C and the five quartic centrifugal distortion constants, the D_{ab} "Coriolis like" operator coefficient, the torsional parameters ρ, V_3, F and three higher order terms (F_ν, d_{ab}, c_2 as defined in Table S2). 105 A and 88 E multiplets corresponding to 300 and 260 hyperfine transitions (mainly the most intense $\Delta F = \Delta J$ transitions) have been fitted, providing a set of determined constants, which allowed the measured MW line frequencies up to $J = 11$ and $K_a = 6$ to be reproduced within the experimental accuracy: RMS (root-mean-square) deviation of 2.1 kHz.

2.2. Room-Temperature mm-Wave Spectrum Assignment

The room-temperature absorption spectrum of 3-NT has been measured in the mm-wave domain (70–220 GHz) using the mm-wave spectrometer of the LPCA Laboratory in Dunkerque (see Section 4.2). Figure 3 shows a 40 GHz wide part of the spectrum and three 40 MHz wide expansions in the 70–110 GHz frequency region. Compared with the MW spectrum simplified by jet-cooled conditions, the room temperature mm-wave spectrum exhibits a quasi-continuum of lines with a complex mixture of A–E components of pure rotational transitions in ground and vibrationally excited states.[28,29] The 40 GHz wide part of the mm-wave spectrum shows this quasi-continuum of lines polluted by saturated lines due to FP effects (see Section 4.2). The observed lines are Doppler limited ($\Delta\nu_{Doppler} \approx 80$ kHz (FWHM)) and artificially broadened by the frequency modulation[30] that limit the spectral resolution to 100 kHz. In these conditions, most of the measured lines are blended and the ^{14}N NQC hyperfine structure could not be resolved at high J values.[31] In the spectral assignment process, molecular parameters extracted from the fit of MW data have been used as initial values to extrapolate, in the 70–220 GHz frequency region, the rotational transitions involving energy levels with $J > 38$. No measurement was performed in the 20–70 GHz range and no transition involving $10 < J < 39$ energy levels were probed.

For the purpose of the present study, two modifications have been made in the BELGI-C_s-hyperfine code: firstly, the code is now able to calculate rotational energy levels up to $J_{max} = 79$ instead of $J_{max} = 30$, allowing 3-NT transitions up to 110 GHz to be assigned; secondly, a treatment of the blended lines as described by Ilyushin et al.[32] was implemented in the program, allowing the measured transitions to be weighted by taking into account their relative intensities.

Line by line assignments were then performed by comparing the experimental and calculated spectra using the SVIEW and ASCP graphical interfaces from the AABS package.[33,34] A routine was developed to convert automatically the input and

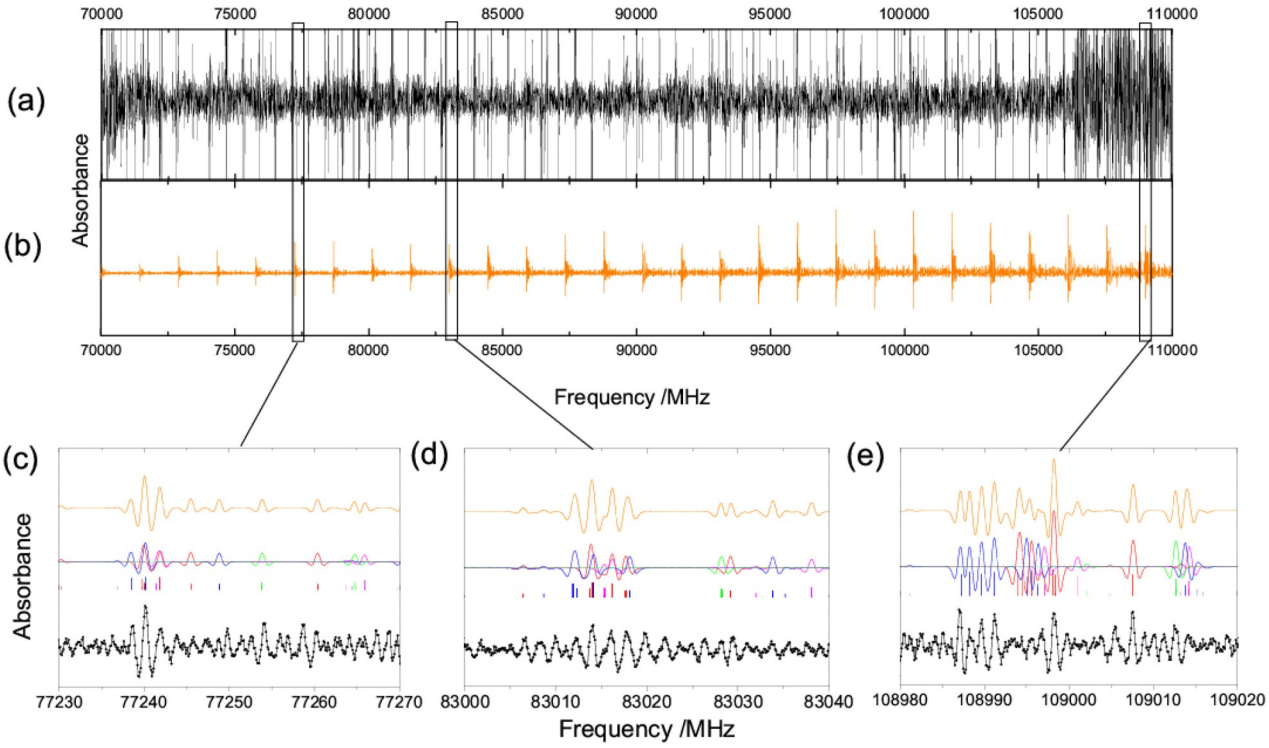

Figure 3. Experimental mm-wave spectrum is compared to the simulated spectrum obtained from the fit. (a) is the 70–110 GHz experimental spectrum (black). (b) is the global simulated spectrum from $v_{t_{CH_3}} = 0$ and $v_{t_{CH_3}} = 1$ states (orange). Some characteristic patterns of 3-NT are presented in (c), (d) and (e): individual contributions of A and E species of $v_{t_{CH_3}} = 0$ (red and blue, respectively) and $v_{t_{CH_3}} = 1$ (pink and green, respectively). All intense saturated spurious patterns in (a) are artefacts due to FP effect (see Section 4.2).

output files of BELGI into Pickett's SPCAT/SPFIT format used in AABS and will be made available to BELGI users.

Despite the complexity of the room temperature mm-wave spectrum, we managed to assign several characteristic features from $v_{t_{CH_3}} = 0$ and $v_{t_{CH_3}} = 1$ even if the A–E splitting are 2 to 5 times larger than those observed in the MW region. The rotational spectrum of the ground state $v_{t_{CH_3}} = 0$ has been analysed up to $J = 74$ and $K_a = 23$. A total of 1222 transitions (705 A and 517 E species) corresponding to 431 blended lines (258 A and 173 E species) are fitted with a RMS deviation of 95.3 kHz corresponding to the experimental accuracy calculated for measured lines with a S/N ratio < 13.[35] The RMS deviation of MW data is slightly improved to 1.9 kHz. In addition, the BELGI-C_s-hyperfine code allows a global fit of the A and E species corresponding to all the torsional levels (ground and torsionally excited states). Therefore, we also assigned rotational lines from the $v_{t_{CH_3}} = 1$ torsional state up to $J = 74$ and $K_a = 9$. A total of 300 transitions in the $v_{t_{CH_3}} = 1$ state (181 A and 119 E species) corresponding to 100 blended lines (50 A and 50 E species) were fitted, resulting in a global fit with a RMS deviation of 98.3 kHz.

The main parameters of the global fit allowing to reproduce the $v_{t_{CH_3}} = 0$ and $v_{t_{CH_3}} = 1$ mm-wave spectrum, presented in Table 1 in the PAM system. The fitted dataset contains all the transitions of $v_{t_{CH_3}} = 0$ state measured in the MW and mm-wave regions as well as the $v_{t_{CH_3}} = 1$ state rotational transitions in the mm-wave region. The complete set of parameters in the RAM system, allowing a room-temperature line list for 3-NT to be built, is presented in Supporting Information (see Table S2). One should note that BELGI-C_s-hyperfine uses only one set of rotational parameters to describe the two torsional states. The result of the global fit including all the assigned transitions is also included in the Supporting Information (see Table S3 and S4 for MW and mm-wave transitions, respectively). In Table 1 the fitted parameters are also compared with the calculated parameters (see Section 4.3). The sixfold V_6 barrier parameter can be determined experimentally because of inclusion of the mm-wave lines in $v_{t_{CH_3}} = 1$. For all the parameters derived from the global fit, the agreement with MP2 calculations is excellent. The quality of the global fit is attested by the unitless standard deviations very close to 1 for both MW and mm-wave data. Numbers of transitions, maximum values of quantum number J''_{max} and associated $K''_{a,max}$, and individual standard deviations (RMS) of $v_{t_{CH_3}} = 0$ and $v_{t_{CH_3}} = 1$ states for A and E species are presented in Table 2; all of the RMS are very close to the experimental accuracy of the MW and mm-wave spectra (2 kHz and 100 kHz, respectively, see Sections 4.1 and 4.2).

As shown in Figure 3c–e, the most intense lines from $v_{t_{CH_3}} = 0$ and $v_{t_{CH_3}} = 1$ states are efficiently reproduced but numerous weaker lines are not reproduced. These remaining lines correspond to rotational transitions involving low-energy levels populated at room temperature of CH_3 and NO_2 torsional states or other low-energy modes measured and computed by Cuisset et al. in Ref. [12]. Table 3 summarises the vibrational wavenumbers of the torsional states for the fundamental and the first overtone calculated with the BELGI-C_s-hyperfine code (for CH_3 torsion) and with quantum chemistry harmonic frequency calculations at the MP2/cc-pVQZ and B98/cc-pVQZ

Table 2. Number N of different transitions included in the global fit, maximum values of quantum number J''_{max} and associated $K''_{a,max}$ value and standard deviation (RMS) of each state ($v_{t_{CH_3}} = 0,1$) and symmetry (A and E species).

		MW				mm-wave			
state	sym	J''_{max}	$K''_{a,max}$	N[a]	RMS [kHz]	J''_{max}	$K''_{a,max}$	N[a]	RMS [kHz]
$v_{t_{CH_3}} = 0$	A	11	6	300	1.8	74	23	705	93.2
$v_{t_{CH_3}} = 0$	E	11	6	260	2.0	73	20	517	96.5
$v_{t_{CH_3}} = 1$	A					74	8	181	116.1
$v_{t_{CH_3}} = 1$	E					74	9	119	109.7

[a] Number of assigned transitions in the fit.

Table 3. Vibrational wavenumbers of the excited torsional states below 100 cm^{-1} predicted from BELGI-C_s-hyperfine ($J = K = 0$) and from harmonic frequency quantum chemistry calculations at the MP2/cc-pVQZ and B98/cc-pVQZ levels of theory. Upper part: positions of the methyl excited torsional states $v_{t_{CH_3}} = 1$ and $v_{t_{CH_3}} = 2$. Lower part: positions of the nitro excited torsional states $v_{t_{NO_2}} = 1$ and $v_{t_{NO_2}} = 2$.

	Unit	BELGI-C_s-hyperfine[a]	MP2/cc-pVQZ harmonic	anharmonic[b]	B98/cc-pVQZ harmonic	anharmonic[b]
CH_3 torsion						
$v_{t_{CH_3}} = 1$	cm^{-1}	27.207	38.380	46.296	16.695	24.611
$v_{t_{CH_3}} = 2$	cm^{-1}	70.244	76.761	100.508	33.389	57.138
NO_2torsion						
$v_{t_{NO_2}} = 1$	cm^{-1}		42.422		48.885	
$v_{t_{NO_2}} = 2$	cm^{-1}		84.844		97.771	

[a] The tabulated values are calculated from a weighted average between A and E species energies ($E_{v_{t_{CH_3}}} = \frac{1}{3}(E_{v_{t_{CH_3}},A} + 2E_{v_{t_{CH_3}},E})$) according to their degeneracy. [b] Anharmonic positions are determined by correcting the calculated harmonic values with empirical anharmonicity constant $\chi_{BELGI} = (\frac{v_{t_{CH_3}}=2}{2}) - (v_{t_{CH_3}} = 1) = 7.916\ cm^{-1}$ obtained from BELGI-C_s-hyperfin $v_{t_{CH_3}} = 1$ and $v_{t_{CH_3}} = 2$ positions.

levels of theory. For such low-frequency, large-amplitude modes, calculations using the VPT2 method usually fail to provide reliable anharmonic frequencies.[36] Nevertheless, by using the BELGI-C_s-hyperfine torsional wavenumbers for $v_{t_{CH_3}} = 1$ and $v_{t_{CH_3}} = 2$, it has been possible to estimate an empirical anharmonic correction (diagonal anharmonicity constant) applied to the calculated harmonic wavenumbers. Harmonic MP2/cc-pVQZ and anharmonic B98/cc-pVQZ are in rather good agreement with the BELGI-C_s-hyperfine vibrational wavenumbers, ensuring the location of excited CH_3 torsional states $v_{t_{CH_3}} = 1$ and $v_{t_{CH_3}} = 2$ around 30 cm^{-1} and 70 cm^{-1}, respectively. Quantum chemistry calculations also estimate the harmonic wavenumbers of the NO_2 torsional mode calculated by B98 and MP2 methods with the cc-pVQZ basis set (see Table 3). Both $v_{t_{NO_2}} = 1$ and $v_{t_{NO_2}} = 2$ are expected below 100 cm^{-1} (45 cm^{-1} for $v_{t_{NO_2}} = 1$ and 90 cm^{-1} for $v_{t_{NO_2}} = 2$). Most of the remaining unassigned rotational lines in the mm-wave spectrum probably originate from $v_{t_{CH_3}} = 2$ methyl torsion and $v_{t_{NO_2}} = 1, 2$ nitro torsion states. Note that for the NO_2 torsion, no splitting of the line are expected because of a high energy barrier to internal rotation ($V_2 \approx 1700$ cm^{-1}).[37]

2.3. Nuclear Quadrupole Coupling Constants

The hyperfine structure due to ^{14}N NQC is clearly observed in the MW spectrum. The two largest diagonal NQC constants χ_{aa} and χ_{cc} were used in the fit to optimise statistical uncertainties, the third diagonal constant χ_{bb} being retrieved from the well-known formula $\chi_{aa}+\chi_{bb}+\chi_{cc}=0$. NQC constants resulting from the BELGI-C_s-hyperfine global fit were converted from RAM into PAM by rotating the NQC matrix around the *z*-axis with the angle θ_{RAM} [see Eq. (8) and Eq. (9)]. These BELGI-C_s-hyperfine NQC values are compared to the NQC constants obtained from the initial fit of the A species by using SPFIT in Table 4. The agreement between the two sets of NQC parameters demonstrates that NQC constants are not perturbed by the internal rotation. The off-diagonal χ_{ab} was kept fixed in SPFIT because only the most intense $\Delta F = \Delta J$ transitions were fitted whereas it was released in BELGI-C_s-hyperfine because of the use of the RAM system rotating the NQC tensor. In Table 4, different sets of calculated NQC constants are also presented. Surprisingly, MP2 and MP2(full) failed in predicting correctly NQC constants, independently from the size of the basis set. However, density functional theory (DFT) methods B2PLYP (recently developed double-hybrid method), B98 (used in this work for calculations of the other molecular parameters) and B3PW91 (suggested by W.C. Bailey, see http://nqcc.wcbailey.net/ and [38]) provide reliable results with relative uncertainties of a few percent. The NQC tensor $\chi_{i,j}$, after conversion from RAM into PAM ($i,j = a,b,c$), has been diagonalised in the principal axes system of the ^{14}N nucleus ($i,j = x,y,z$) to link the NQC constants to the molecular geometry and to the electronic structure ($\chi_{i,j} = eQq_{ij}$ with *e* the electric charge of the proton, *Q* the quadrupole moment, and q_{ij} the molecular electric field gradient). This diagonalisation implies the calculation of the α angle between the principal axis α of the molecule and the principal axis *z* of the nucleus oriented, in a first approximation, along the internuclear axis C-N.[39,40] The α values, determined both from experimental and calculated NQC parameters, are in good agreement. Finally, the electric field gradient orientation can be evaluated with the asymmetry parameter $\eta = \frac{\chi_{xx}-\chi_{yy}}{\chi_{zz}}$. In Table 4, the experimental and calculated values of η indicate a strong deviation of the electric field gradient from the usually admitted cylindrical symmetry around the *z*-axis almost coincident with the C–N bond. Indeed, the two experimental η values are very close to 0.45 and the calculated η values are always >0.5. This specificity is probably due to the NO_2 functional group characterised with a partial double-bond contribution (unlocalised electron); from the point of view of NQC, the nitrogen in NO_2 behaves as if it is quadruply bonded to a dummy atom (the two oxygen) of lower electronegativity.[41,42] This should strongly perturb the electronic distribution around the quadrupolar nucleus, which may explain the failure of "localised electrons" methods such as MP2 to predict NQC constants.

Table 4. Fitted and calcu[lated nuclear quadrupole coupling constants $\chi_{i,j}$ in the principal axes system ($i,j = a,b,c$) with their standard deviations in the last digits, diagonalized $\chi_{i,j}$ in the principal axes system of the ^{14}N nucleus ($i,j = x,y,z$), asymmetry parameter η and angle α between *a* and *z* axes calculated for each set of parameters with their differential uncertainties on the last digit.

	Unit	BELGIC$_s$-hyperfine	SPFIT	B98	B2PLYP(full)	B3PW91	MP2	MP2(full)
		(PAM)	(PAM)	cc-pVQZ	cc-pVTZ	6-311 + G(df,pd)	cc-pVQZ	cc-pVTZ
χ_{aa}	MHz	−1.0494(16)	−1.0460(21)	−1.244	−0.9898	−1.1151	−0.664	−0.6287
χ_{bb}	MHz	0.1986(91)[a]	0.1947(47)[a]	-0.082	0.1360	0.0627	0.6028	0.5419
χ_{cc}	MHz	0.8507(20)	0.8513(26)	1.326	0.8539	1.0523	0.0637	0.0867
χ_{ab}	MHz	(−)0.4106(31)[b]	[−0.4247][b]	−0.388	−0.4296	−0.3937	−0.4247	−0.3913
χ_{xx}	MHz	0.3244(102)	0.3261(45)	0.036	0.281	0.182	0.064	0.087
χ_{yy}	MHz	0.8507(20)	0.8513(26)	1.326	0.854	1.052	0.732	0.661
χ_{zz}	MHz	−1.17507(50)	−1.1775(24)	−1.362	−1.135	−1.235	−0.793	−0.747
η[c]	unitless	0.4479(106)	0.4461(69)	0.947	0.505	0.704	0.842	0.768
α[d]	deg	16.831(263)	17.198(108)	16.868	18.675	16.882	16.921	16.882

[a] Calculated according to $\chi_{aa}+\chi_{bb}+\chi_{cc}=0$, standard deviation has been indirectly obtained from standard deviation of χ_{aa} and χ_{cc}. [b] Fixed to calculated value in SPFIT but released in BELGIC$_s$-hyperfine, see text for details. [c] Asymmetry parameter $\eta = \frac{\chi_{xx}-\chi_{yy}}{\chi_{zz}}$. [d] Angle between the principal axis *a* of the molecule and the principal axis *z* of the quadrupolar nucleus from diagonalisation of the χ matrix.

2.4. Internal Rotation Potential

The determination of the internal rotation parameters permits the threefold internal rotation potential of the methyl group to be characterised. The energy levels of the A and E species in the ground state are presented in Figure 4 as a function of J (top x-axis). In the same Figure, the internal rotation potential is also represented as a function of the torsional angle (bottom x-axis). The potential barrier V_3 is very low and the methyl group is in an almost free rotation regime, this extreme limit has allowed the BELGI-C_s-hyperfine model to be tested with success. All the E species rotational energy levels lie above the barrier. For A species, only the $J<6$ levels have an energy below the barrier. Such a small energy barrier characterised the internal rotation potential of methyl groups for *meta* and *para* isomeric forms of toluene derivatives. Indeed, the barrier to methyl internal rotation is very sensitive to the steric and electronic surroundings of the top. A more symmetric electron density around the carbon to which the -CH_3 group is attached generally leads to lower barriers to internal rotation.[43] Therefore, for *ortho* toluene derivatives, the V_3 barrier is significantly bigger, typically several hundreds of wavenumber units (e.g. $\approx$ 200 cm^{-1} for 2-toluidine; $\approx$ 700 cm^{-1} for 2-tolunitrile).[44] In Table 5, $V_{3,6}$ barrier parameters determined in *meta* isomeric forms of mono-substituted toluene derivatives are compared to our experimental results on 3-NT. Depending on the molecule, the values of V_3 and V_6 have been fitted from MW rotational measurements[45–47] or fitted and/or calculated from fluorescence excitation spectra.[43,44,48] The value of the V_3 barrier of 3-NT is interleaved between that of 3-xylene and 3-toluidine where the quasi free internal rotation is hindered by a methyl and an amino group, respectively. Nevertheless, for such low barriers, the V_3 values are rather close and their level of accuracy and are therefore very important if we want to probe the CH_3 group molecular surrounding from the barrier height. With relative accuracies better than 1%, the fitted barrier parameters of 3-NT reach a level of accuracy significantly better than the others. In particular, the small V_6 correction is well determined providing a $\frac{V_6}{V_3}$ ratio of $(3.45\pm0.03)\times10^{-3}$. This ratio is low and suggests that the electronic distribution around the methyl group is weakly affected by the NO_2 group.

Table 5. Barrier parameters of the internal methyl rotation in *meta* isomeric form of mono-substituted toluene derivatives.

Molecule	Substituent	V_3 [cm^{-1}]	V_6 [cm^{-1}]	Experimental Method
toluene	–	–	4.83783617(94)	MW spectroscopy[23,45]
m-xylene	-CH_3	4.49(13)	–	FTMW spectroscopy[49]
***m*-nitrotoluene**	**-NO_2**	**6.7659(24)**	**0.02333(22)**	**this work**
m-toluidine	-NH_2	9	−10	fluorescence spectroscopy[48]
m-tolunitrile	-CN	13.58(23)	−13.68(560)	rovibronic spectroscopy[44]
m-cresol-OD(*trans*)	-OD	3.188(180)	–	rovibronic spectroscopy[43]
m-cresol-OD(*cis*)	-OD	21.341(52)	–	rovibronic spectroscopy[43]
m-fluorotoluene	-F	15.8(1)	7.97(17)	MW spectroscopy[47]

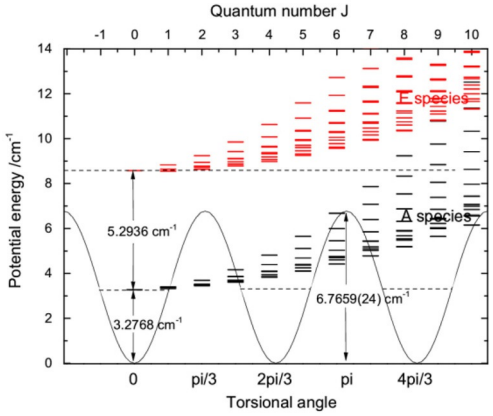

Figure 4. Threefold internal rotation potential of the methyl group calculated with experimental V_3 and V_6 values, showing three equivalent positions along the torsional angle (bottom x-axis). Energy levels of the A and E species in the ground state are presented in black and red, respectively, up to $J=10$ (top x-axis).

The evolution of the A–E splittings with J and K_a quantum numbers are plotted in Figure 5 for $v_{t_{CH_3}}=0$ a-type and b-type transitions involving rotational energy levels with $0<J<60$ and $0<K_a<14$. Quantum number label problems appear for high J and K_a quantum numbers with the BELGI-C_s-hyperfine code when the eigenfunctions are strongly mixed. For each K_a series, the J dependence of the A–E splitting shows some characteristic features with minima and maxima observed in different molecules with CH_3 internal rotation.[50] These extrema show a linear dependence in J and the A–E splitting varies from hundreds of MHz (a-type transitions) to more than 10 GHz (b-type transitions). We note that the largest splittings are observed for transitions involving low energy levels with $J\approx 4K_a$ both for a-type and b-type transitions.

2.5. Limitations of the Model

In this study, the first limitation was computational: the fit of $v_{t_{CH_3}}=0$ and $v_{t_{CH_3}}=1$ was performed for rotational transitions up to $J=79$ only due to the high computational memory cost required by the BELGI-C_s-hyperfine two-step diagonalisation. Whereas the first diagonalisation of the Hamiltonian is performed on a size-limited matrix (21×21) without any dependence on J, the second diagonalisation (yielding the rotation, centrifugal distortion, and rotation-torsion coupling terms) is performed on a $9(2J+1)\times9(2J+1)$ dimensional matrix (see Ref. [26] and references therein).

The second limitation of the model occurs for energy levels involving high J and K_a quantum numbers when the wave functions begin to mix with each other, which leads to label

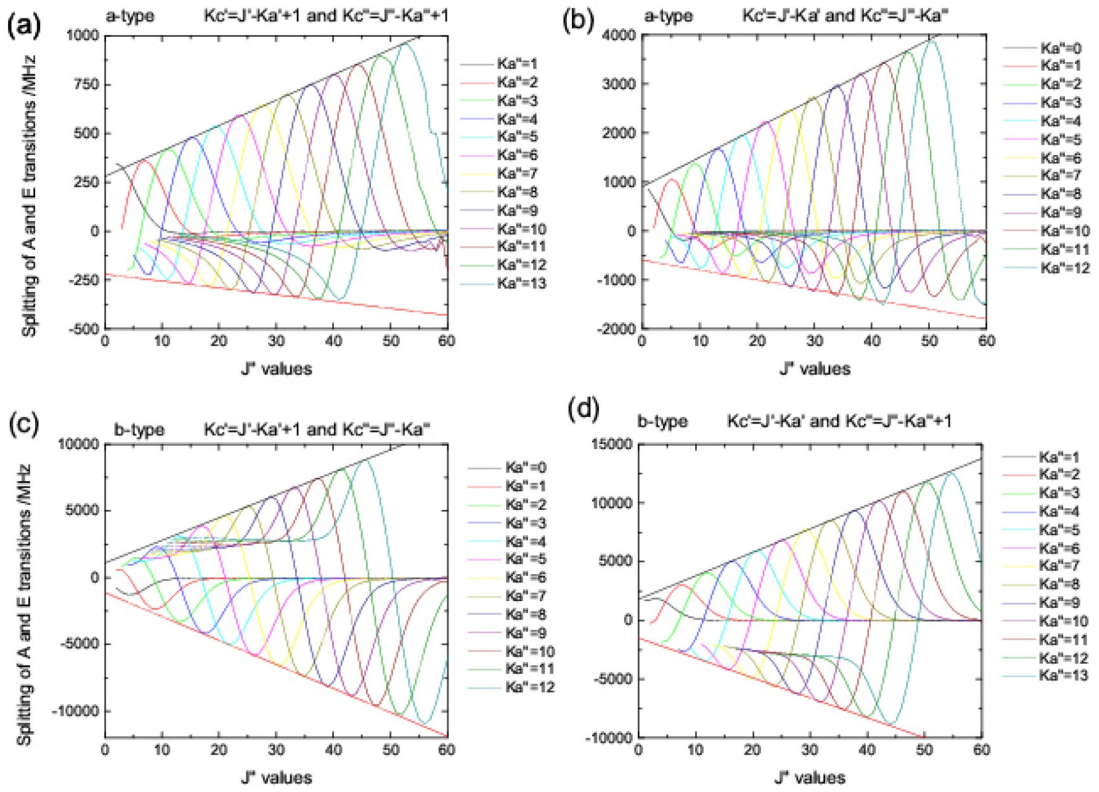

Figure 5. Splittings of the A and E species rotational transitions in the ground state up to $J=79$ and $K_a=13$. Different series are presented for R branches: (a) a-type transitions for $K'_c = J' - K'_a + 1$ and $K''_c = J'' - K''_a + 1$, (b) a-type transitions for $K'_c = J' - K'_a$ and $K''_c = J''e - K''_a$, (c) b-type transitions for $K'_c = J' - K'_a + 1$ and $K''_c = J'' - K''_a$, and (d) b-type transitions for $K'_c = J' - K'_a$ and $K''_c = J'' - K''_a + 1$. The minimal and maximal splittings show a linearity indicated by red and black slopes, respectively.

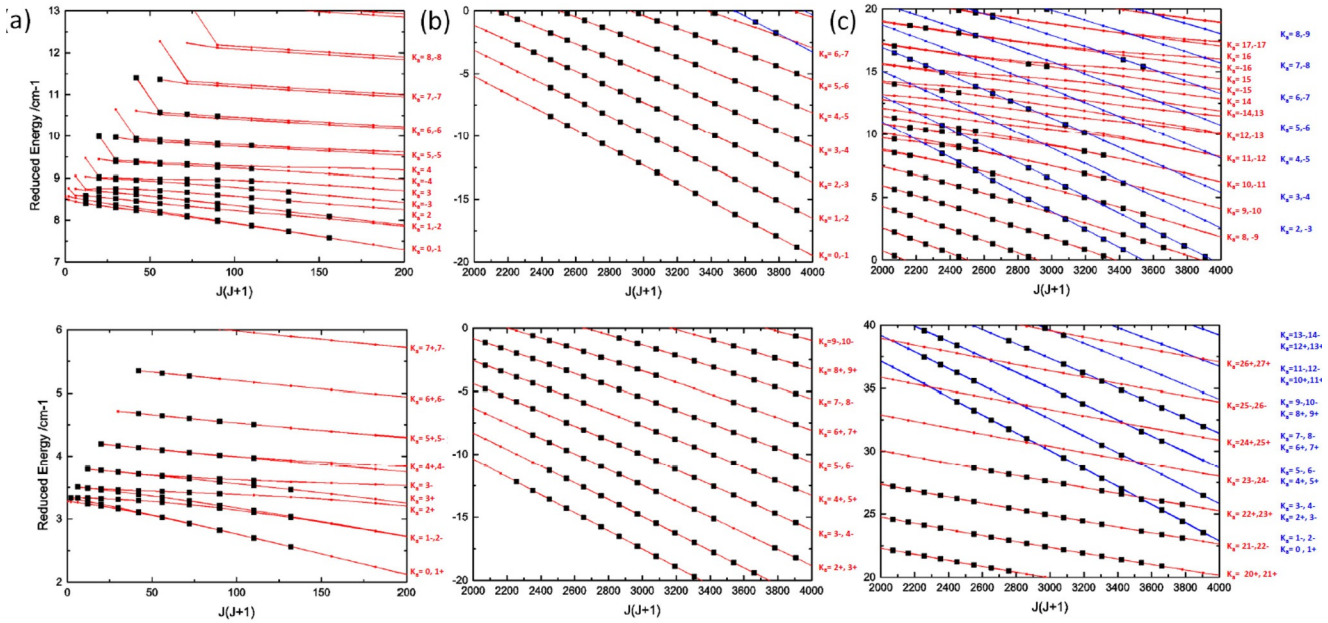

Figure 6. Calculated rotational energies in $v_{t_{CH_3}} = 0$ (red linked dots) and $v_{t_{CH_3}} = 1$ (blue linked dots) up to $J=63$. The reduced energies $E-B^{(v)}J(J+1)$ have been used instead of E for clarity. Black dots belong to the reduced energy levels involved in assigned experimental transitions and labels correspond to K_a values. Three part are presented: (a) MW analysis, (b) mm-wave analysis of $v_{t_{CH_3}} = 0$ and (c) mm-wave analysis of $v_{t_{CH_3}} = 0$ and $v_{t_{CH_3}} = 1$. The A species (bottom graphs) and E species (top graphs) are presented separately.

problems and gives the possibility to local interactions (e.g. avoided crossing) between energy levels.[51] The Figure 6 illustrates this last point. The calculated reduced rotational energy levels are presented as a function of $J(J+1)$. A and E species have different symmetry and therefore cannot interact with each other, so they are presented separately for clarity. The K_a series have been identified to discuss the limits of assignments and the possible interactions. The labelling is performed according to positive and negative K_a values considered by the BELGI-C_s-hyperfine code. Although J, K_a and K_c are good quantum numbers to describe the A species, it was shown that the meaning of K_c labels of the E species must be based on something other than symmetry properties.[26] For this reason, a specific label of the rotational energy levels for A and E species has been proposed by I. Kleiner in Ref. [26].

In Figure 6 (bottom part), energy levels of A species are labelled with J, $K_a\pm$ with $\pm$ the "parity" quantum number. If K_a is even, K_a+ and K_a- values correspond to $K_c=J-K_a$ and $K_c=J-K_a+1$, respectively, and vice versa if K_a is odd. In Figure 6 (upper part), the $\pm K_a$ labels of E species are associated with $K_c=J-K_a$ and $K_c=J-K_a+1$ levels with $E_{J-K_a+1} > E_{J-K_a}$.[18] Three regions of the reduced energy levels have been selected: the first region (a) corresponds to low K_a and J energy levels probed by MW spectroscopy, the second region (b) corresponds to $v_{t_{CH_3}}=0$ energy levels probed by mm-wave spectroscopy, and the third region (c) corresponds to higher energy $v_{t_{CH_3}}=0$ and $v_{t_{CH_3}}=1$ levels mixed with each other. In region (a), low J and low K_a levels are assigned both for A and E species. Most of the levels become doubly degenerated for $J(J+1)>200$, with a different degeneracy observed for low and high K_a values (lowest energy levels are degenerated with the same K_c values but the highest energy levels are degenerated with the same K_a values for A species). In region (b), the most of represented energy levels are involved in experimental transitions. The presence of unassigned levels is simply due to experimental artefacts (overlapping with intense FP effects; see Section 4.2). All series are doubly degenerated, both for A and E species. For A species, the degenerated levels are levels with the same K_c and different K_a. Finally, in region (c) crossed series are observed between the two states $v_{t_{CH_3}}=0$ and $v_{t_{CH_3}}=1$ and consequently numerous levels cannot be assigned, highlighting some limitations of the model. For $v_{t_{CH_3}}=1$, label problems occur and it was not possible to assign transitions involving energy levels with $K_a>8$. As pointed out by Ilyushin et al.,[24] a harmonic oscillator vibrational quantum number $v_{t_{CH_3}}$ is not well defined for levels above the barrier and a free-rotor quantum number m is not well defined for levels below the barrier. Given that, in the present case, we deal with a very low threefold barrier, the free-rotor quantum number m should be more appropriate than $v_{t_{CH_3}}$ in high torsional states.

We can also mention the possible interaction between $v_{t_{CH_3}}=1$ and $v_{t_{CH_3}}=2$ for A species because their band origins are expected to be very close in energy (0.11 cm^{-1} predicted from BELGI-C_s-hyperfine by taking into account the characteristics of the barrier). It may be assumed that the unassigned lines can be associated with $v_{t_{CH_3}} \geq 2$ states or to other low-frequency vibrationally excited modes, such as the NO_2 torsion ($v_{t_{NO_2}}$ mode), which are not studied here (see Section 4.2, Table 3).

3. Conclusions

The challenging high-resolution measurements and analysis of 3-NT, one of the TNT explosive taggants, have been performed for the first time under jet-cooled conditions in the MW region and at room temperature in the mm-wave region, providing a rotational line list that can be used for future gas-phase in situ detection. Both experimental and theoretical difficulties have been overcome: a weak and congested rotational spectrum at room temperature has been measured and energy levels perturbed by a very low internal rotation barrier have been calculated. An internal rotation potential function of the methyl group has been determined from the spectroscopic analysis. A very low barrier has been derived from the $v_{t_{CH_3}}=0,1$ global fit with an excellent accuracy ($V_3=6.7659(24)$ cm^{-1} and $\frac{V_6}{V_3}=0.00345(3)$). The computational and physical limitations of the model have been discussed. Structural properties of 3-NT have been derived from the spectroscopic analysis of the C–CH_3 and C–NO_2 bond, with both being in the (a,b) plane. The resolved hyperfine structure in the MW region allowed the angle between the C–NO_2 bond and the a-axis to be determined ($\alpha=16.66(32)^\circ$). On the other hand, the $\theta=-19.18639(74)^\circ$ angle determined from the RAM into PAM conversion of the rotational parameters permits the angle between the C–CH_3 bond and the a-axis to be determined ($\angle(i,a)=-43.3346(17)^\circ$). For 3-NT, a complete rotational line list up to 110 GHz with transition frequency accuracies better than 100 kHz is now available (see Tables S3 and S4 in the Supporting Information) and constitutes a crucial tool for future in situ detection in the gas phase. A similar study for 2-NT and 4-NT is in progress to examine the influence of the isomeric form on the internal rotation potential and to give the opportunity to identify a specific taggant in a mixture of the different isomers as was demonstrated in the far-infrared with vibrational fingerprints.[28]

4. Experimental and Theoretical Methods

4.1. FP-FTMW Spectroscopy Experiments

In this work, the FP-FTMW technique coupled to a pulsed supersonic jet was used.[42,46,52] A heated nozzle[53] allowed the 3-NT vapour to be mixed with the carrier gas (neon) at a backing pressure of about 0.2 MPa. Temperatures ranging from 373 K to 393 K were found to optimise the signal-to-noise ratio (S/N) depending on the amplitude of recorded lines. The mixture was introduced into a FP cavity through a series 9 General Valve pin hole nozzle (0.8 mm) at a repetition rate of 1.5 Hz. Jet-cooled molecules (T_{rot} of a few K) were polarised within the supersonic expansion by a 2 μs pulse. The free-induction decay (FID) signal was recorded using heterodyne detection at 30 MHz, and was digitised at a repetition rate of 120 MHz on a 14 bit resolution electronic card. FID signals were accumulated between 50 and 1000 times, depending on the line intensity, to obtain the best S/N ratio. After transformation of the average time domain signals, lines of the amplitude spectrum

were observed as Doppler doublets due to the coaxial arrangement of the jet and the Fabry–Pérot cavity. Each resonance frequency was measured as the average frequency of the two Doppler components. The spectral resolution depended on the number of recorded points. The frequency grid was set to 1.8 kHz, which was found to be sufficient because the Doppler linewidths should be of several kHz. According to this value, the experimental accuracy of the MW measured lines was fixed to 2 kHz for the fit.

4.2. Millimeter-Wave Spectroscopy Experiment

The room-temperature absorption spectrum of 3-NT has been measured in the mm-wave domain (70–220 GHz). A continuous flow of 0.8 Pa of the sample, maintained by a roughing pumping, was passed through a 125 cm-long and 56 mm-diameter single path stainless steel absorption cell equipped with Teflon windows and probed by the radiation generated by a frequency multiplier chain (Virginia Diodes, Inc). Two off-axis parabolic mirrors are used to collimate the radiation into the cell and then to refocus it into a liquid-helium-cooled InSb bolometer.[30] The spectrum has been recorded in 2F frequency modulation by using a frequency modulation of 10 kHz, 40 kHz modulation depth of the frequencies delivered by the synthesiser, a time constant of 200 ms and 100 kHz frequency steps. The very dense and weak spectrum was complicated by the presence of many excited states lines at room temperature and by the congestion of the lines, which are mostly blended.

Moreover, compared with the weak intensity of 3-NT lines, strong peaks are observed in the mm-wave spectrum due to Fabry–Pérot (FP) effects. Two FP effects are observed with two different free spectral ranges (FSR) of 118 MHz and 624 MHz due to stationary waves between the two windows of the cell and between the source and the cell, respectively. The first one has an amplitude and a width around 50 times larger than the molecular intensities and linewidths, respectively. This FP effect is easily removed by using a low pass FFT filter subtracted from the spectrum (see Figure 7). The second FP effect has a width of 1 MHz very close to the molecular linewidth. In this case, it was not possible to remove it with the FFT filter without affecting the shape of the very weak molecular transitions. This FP effect can be seen in the spectrum shown in Figure 3a. The experimental error of measured line frequencies was estimated to about 100 kHz using Equation (2) of Ref. [35] taking into account the S/N ratio, the frequency step and the molecular linewidth.

Given that the spectrum was very dense and weak, the 99% purity of the Sigma–Aldrich product was verified by using a gas chromatography-mass spectrometer (GC-MS): negligible traces of 2-NT (0.2%) and 4-NT (0.7%) were identified. After several days of room-light exposition, the liquid-phase 3-NT became browner because of a dimerisation and trimerisation of the product, as revealed by GC-MS and nuclear magnetic resonance (NMR) measurements. The polymerization of the molecule presents no contribution in the rotational spectrum.

4.3. Theoretical Methods

All the calculations were performed using Gaussian 09 (Revision D.01) software[54] on the computing cluster of PhLAM laboratory. The frozen-core approximation was used throughout. Dunning and co-workers correlation consistent basis set cc-pVXZ (X = D, T, Q) were used.[55] All geometries were fully optimised at the MP2 and B98 levels using the tight convergence criterion. Extrapolations to complete basis set (CBS) for energies (including ZPE corrections) and rotational constants were performed using Dunning's formula.[56] Frequencies and ground state (v = 0) rotational constants were calculated at the anharmonic level (VPT2 calculations as implemented in the Gaussian software)[57] with a tight SCF convergence criterion and the ultrafine integral grid option. Anharmonic corrections have been extrapolated from DFT (B98) to the MP2 level by following a method suggested by Barone et al.[36] and recently successful in the case of various systems[58,59] (denoted "hybrid" hereafter). Briefly, given that anharmonic calculations at the MP2 level are hardly affordable for such a relatively large molecule, rotational constants of a given vibrational state v (called "hybrid") are estimated by adding DFT anharmonicity (B98/CBS) to the MP2 constants at equilibrium (MP2/CBS) [Eqs. (1), (2), and (3)]:

$$A_v^{\text{hybrid}} = A_{\text{eq}}^{MP2} - \left(A_{\text{eq}}^{B98} - A_v^{B98}\right) \quad (1)$$

$$B_v^{\text{hybrid}} = B_{\text{eq}}^{MP2} - \left(B_{\text{eq}}^{B98} - B_v^{B98}\right) \quad (2)$$

$$C_v^{\text{hybrid}} = C_{\text{eq}}^{MP2} - \left(C_{\text{eq}}^{B98} - C_v^{B98}\right) \quad (3)$$

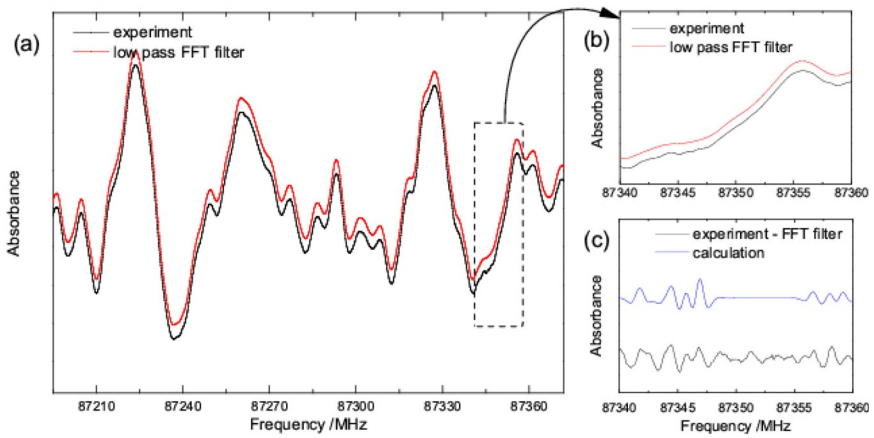

Figure 7. (a) Part of the observed mm-wave spectrum in the 87.3 GHz frequency region (black) with the low-pass FFT filter which reproduce the strong FP effect (red), the curves have been shifted in intensity for better readability, (b) Zoom on a 20 MHz wide region and (c) the difference between the experimental spectrum and the FFT filter (black) is compared to the calculated spectrum (blue).

where A_ν, B_ν and C_ν the rotational constant of the vibrational state ν and A_{eq}, B_{eq} and C_{eq} is the rotational constant at equilibrium.

To have an initial prediction of the frequency positions of the A–E components, it is necessary to have a first estimation of the torsional parameters V_3, F and ρ. These parameters correspond to the barrier height of the internal rotation potential of CH_3, the internal rotation constant, and a coupling constant between rotation and torsion, respectively.[22] The potential function is expressed as a Fourier series in terms of the torsional angle α [Eq. (4)]:

$$V(\alpha) = 1/2V_3(1-\cos(3\alpha)) + 1/2V_6(1-\cos(6\alpha)) \quad (4)$$

The first term in Equation (4) includes the barrier height V_3 and its value was estimated at the MP2/CBS level by optimising the transition state of the methyl group rotation and ZPE corrected from harmonic frequency calculations at equilibrium and transition state geometries. With three equivalent positions of the CH_3 group in relation to the molecular frame, the second term involving V_6 may be neglected in the $v_{t,CH_3} = 0$ ground-state analysis. The internal rotation constant F and the ρ_g components of the ρ vector are related to the principal moments of inertia of the molecule $I_g = I_a$, I_b and I_c and to the moment of inertia of the top I_α by the expressions given in Equation (5):

$$\rho_g = \lambda_g \frac{I_\alpha}{I_g} \qquad F = \frac{\hbar^2}{2rI_\alpha} \qquad r = 1 - \sum_g \lambda_g^2 \frac{I_\alpha}{I_g} \quad (5)$$

where λ_g is the direction cosines of the internal rotation axis i of the top in the principal axis system; that is, $\lambda_g = \cos(\theta(i,g))$ with $g = a,b,c$. From the 3-NT equilibrium structure optimised at the MP2/cc-pVQZ level of theory, calculated values of ρ and F are estimated and used as initial parameters to predict the splitting due to internal rotation. In addition, the rotational constants were corrected with a perturbation approach according to D. R. Herschbach[60] to take into account the coupling between the global rotation of 3-NT and the internal rotation of the methyl group. A second-order perturbation is therefore introduced to correct the hybrid constants A_0^{hybrid} and B_0^{hybrid} of $v_{t_{CH_3}} = 0$ state following the Herschbach Equations (6) and (7):

$$A_{0\sigma}^{corr.} = A_0^{hybrid} + FW_{0\sigma}^{(2)} \left(\lambda_a \frac{I_\alpha}{I_a}\right)^2 \quad (6)$$

$$B_{0\sigma}^{corr.} = B_0^{hybrid} + FW_{0\sigma}^{(2)} \left(\lambda_b \frac{I_\alpha}{I_b}\right)^2 \quad (7)$$

$W_{0\sigma}^{(2)}$ is a dimensionless perturbation coefficient estimated from the reduced barrier $s = \frac{4V_3}{9F}$ for a given torsional level ($v_{t,CH_3} = 0$) and A ($\sigma = 0$) or E ($\sigma = \pm 1$) state. In Ref. [60], the values of $W_{0\sigma}^{(2)}$ for a second-order perturbation are tabulated for $8 \le s \le 100$. We found $W_{00}^{(2)} = 0.6532$ and $W_{0\pm1}^{(2)} = -0.3130$ by extrapolating the tabulated values for a very small reduced barrier ($s < M > 1$ for 3-NT).

Then, for a complete correction, an averaged correction of A and E species from D. R. Herschbach formalism is applied, leading to $A_0^{corr.} = 0.5*(A_{00}^{corr.} + A_{0\pm1}^{corr.})$ and $B_0^{corr.} = 0.5*(B_{00}^{corr.} + B_{0\pm1}^{corr.})$, C_0^{hybrid} value is kept as it is not affected by internal rotation.

Concerning NQC constants, given that large differences were observed between MP2 and B98 results, additional calculations were performed to obtain the best characterisation of the electric field gradient tensor induced by the coupling with the ^{14}N nuclear spin. B2PLYP, B3PW91 and MP2(full) levels of theory have been tested with specific basis-set (see Table 4) and compared to the experimental parameters obtained from the fit of MW data.

Finally, rotational constants, dipole moment components and NQC constants calculated in the PAM system have to be converted into the RAM system for use in the BELGI-hyperfine code. These conversions from PAM into RAM are performed using the rotation matrix $R_c(\theta_{RAM})$ [Eq. (8)]:

$$R_c(\theta_{RAM}) = \begin{pmatrix} \cos(\theta_{RAM}) & -\sin(\theta_{RAM}) & 0 \\ \sin(\theta_{RAM}) & \cos(\theta_{RAM}) & 0 \\ 0 & 0 & 1 \end{pmatrix} \quad (8)$$

where θ_{RAM} is the angle between the PAM and RAM systems around the c-axis. It can be calculated from the optimized equilibrium geometry using the Equation (9):

$$tan\theta_{RAM} = \frac{\lambda_b I_a}{\lambda_a I_b} \quad (9)$$

We can note that the angle $\angle(i,a)$ between the a-axis and the internal axis i along the C–CH_3 bond may be determined from the optimised equilibrium geometry using the direction cosines [Eq. (10)]:

$$tan\angle(i,a) = \frac{\lambda_b}{\lambda_a} = \frac{I_b}{I_a} tan\theta_{RAM} \quad (10)$$

All the calculated parameters used in Section 4.3 are detailed in the Supporting Information (see Table S1).

Acknowledgements

We thank the Ph.D. financial support of A. Roucou; that is, the region Hauts-de-France and the French Direction Générale de l'Armement (DGA), and the Ph.D. financial support of S. Bteich; that is, the region Hauts-de-France and the Laboratory of Excellence CaPPA (Chemical and Physical Properties of the Atmosphere). A. Roucou was funded by the "Groupe de Recherche GdR CNRS SPECMO" to visit I. Kleiner in LISA, Créteil and he was awarded an EOLE fellowship (excellence scholarship of the Franco-Dutch network) which permitted him to visit W. L. Meerts at Radboud Universiteit, Nijmegen, The Netherlands. The mm-wave spectrometer has been supported by the French "Délégation Générale pour l'Armement" (Projet de Recherche Exploratoire et Innovation No. 06.34.037). The authors are grateful to: - Dr. F. Cazier and Dr. F. Delattre from, respectively, the Centre Commun de Mesures (CCM) and the Unité de Chimie Environnementale et Interactions sur le Vivant (UCEIV) of the Université du Littoral Côte dOpale for the GC-MS and NMR measurements. - Pr. Wolfgang Stahl from RWTH Aachen University for a private communication, which permit to modify the input file of BELGI-C_s-hyperfin from $J_{max} = 30$ to $J_{max} = 79$ and Dr. Guillaume Dhont for the implementation of the program on the CALCULCO server - Pr. D. A. Sadovskii for its fruitful discussions on the 3-NT rotational energy level patterns.

Conflict of interest

The authors declare no conflict of interest.

Keywords: analytical methods · internal rotation · quantum chemistry · rotational spectroscopy · trace analysis

[1] H. Östmark, S. Wallin, H. G. Ang, *Propellants Explos. Pyrotech.* **2012**, *37*, 12 – 23.
[2] D. S. Moore, *Rev. Sci. Instrum.* **2004**, *75*, 2499 – 2512.
[3] A. R. Krause, C. Van Neste, L. Senesac, T. Thundat, E. Finot, *J. Appl. Phys.* **2008**, *103*, 094906.
[4] M. Snels, T. Venezia, L. Belfiore, *Chem. Phys. Lett.* **2010**, *489*, 134 – 140.
[5] R. Prasad, R. Prasad, G. Bhar, S. Thakur, *Spectrochim. Acta Part A* **2002**, *58*, 3093 – 3102.
[6] A. G. Mercado, J. A. Janni, B. Gilbert in *European Symposium on Optics for Environmental and Public Safety*, International Society for Optics and Photonics, **1995**, pp. 142 – 152.
[7] D. Wu, J. P. Singh, F. Y. Yueh, D. L. Monts, *Appl. Opt.* **1996**, *35*, 3998 – 4003.
[8] C. Mullen, A. Irwin, B. V. Pond, D. L. Huestis, M. J. Coggiola, H. Oser, *Anal. Chem.* **2006**, *78*, 3807 – 3814.
[9] H. Diez-y-Riega, R. Gunawidjaja, H. Eilers, *J. Photochem. Photobiol. A* **2013**, *268*, 50 – 57.
[10] J. D. Rodgers, N. J. Bunce, *Environ. Sci. Technol.* **2001**, *35*, 406 – 410.
[11] J. A. Widegren, T. J. Bruno, *J. Chem. Eng. Data* **2010**, *55*, 159 – 164.
[12] A. Cuisset, S. Gruet, O. Pirali, T. Chamaillé, G. Mouret, *Spectrochim. Acta Part A* **2014**, *132*, 838 – 845.
[13] M. Cirtog, P. Asselin, P. Soulard, B. Tremblay, B. Madebène, M. E. Alikhani, R. Georges, A. Moudens, M. Goubet, T. R. Huet, O. Pirali, P. Roy, *J. Phys. Chem. A* **2011**, *115*, 2523 – 2532.
[14] J. H. Høg, L. Nygaard, G. O. Sørensen, *J. Mol. Struct.* **1971**, *7*, 111 – 121.
[15] V. V. Ilyushin, E. Alekseev, S. Dyubko, I. Kleiner, J. T. Hougen, *J. Mol. Spectrosc.* **2004**, *227*, 115 – 139.
[16] R. Kannengiesser, W. Stahl, H. V. L. Nguyen, I. Kleiner, *J. Phys. Chem. A* **2016**, *120*, 3992 – 3997.
[17] R. J. Foltynowicz, R. E. Allman, E. Zuckerman, *Chem. Phys. Lett.* **2006**, *431*, 34 – 38.
[18] J. T. Hougen, I. Kleiner, M. Godefroid, *J. Mol. Spectrosc.* **1994**, *163*, 559 – 586.
[19] S. Kassi, D. Petitprez, G. Wlodarczak, *J. Mol. Struct.* **2000**, *517 – 518*, 375 – 386.
[20] M. Tudorie, L. H. Coudert, T. R. Huet, D. Jegouso, G. Sedes, *J. Chem. Phys.* **2011**, *134*, 074314.
[21] H. Dreizler, *Z. Naturforsch. A* **1961**, *16*, 1354 – 1367.
[22] C. C. Lin, J. D. Swalen, *Rev. Mod. Phys.* **1959**, *31*, 841.
[23] V. V. Ilyushin, Z. Kisiel, L. Pszczolkowski, H. Mäder, J. T. Hougen, *J. Mol. Spectrosc.* **2010**, *259*, 26 – 38.
[24] V. V. Ilyushin, R. Rizzato, L. Evangelisti, G. Feng, A. Maris, S. Melandri, W. Caminati, *J. Mol. Spectrosc.* **2011**, *267*, 186 – 190.
[25] H. M. Pickett, *J. Mol. Spectrosc.* **1991**, *148*, 371 – 377.
[26] I. Kleiner, *J. Mol. Spectrosc.* **2010**, *260*, 1 – 18.
[27] D. Jelisavac, D. C. Gómez, H. Nguyen, L. Sutikdja, W. Stahl, I. Kleiner, *J. Mol. Spectrosc.* **2009**, *257*, 111 – 115.
[28] A. Cuisset, M. A. Martin-Drumel, F. Hindle, G. Mouret, D. A. Sadovskii, *Chem. Phys. Lett.* **2013**, *586*, 10 – 15.
[29] A. Roucou, G. Dhont, A. Cuisset, M. A. Martin-Drumel, S. Thorwirth, D. Fontanari, W. L. Meerts, *J. Chem. Phys.* **2017**, *147*, 054303.
[30] G. Mouret, M. Guinet, A. Cuisset, L. Croize, S. Eliet, R. Bocquet, F. Hindle, *IEEE Sens. J.* **2013**, *13*, 133 – 138.
[31] O. Pirali, Z. Kisiel, M. Goubet, S. Gruet, M. A. Martin-Drumel, A. Cuisset, F. Hindle, G. Mouret, *J. Chem. Phys.* **2015**, *142*, 104310.
[32] V. Ilyushin, A. Kryvda, E. Alekseev, *J. Mol. Spectrosc.* **2009**, *255*, 32 – 38.
[33] Z. Kisiel, E. Białkowska-Jaworska, L. Pszczółkowski, *J. Chem. Phys.* **1998**, *109*, 10263 – 10272.
[34] Z. Kisiel, E. Białkowska-Jaworska, L. Pszczółkowski, *J. Mol. Spectrosc.* **2000**, *199*, 5 – 12.
[35] M. Martin-Drumel, F. Hindle, G. Mouret, A. Cuisset, J. Cernicharo, *Astrophys. J.* **2015**, *799*, 115.
[36] M. Biczysko, P. Panek, G. Scalmani, J. Bloino, V. Barone, *J. Chem. Theory Comput.* **2010**, *6*, 2115 – 2125.
[37] N. W. Larsen, *J. Mol. Struct.* **2010**, *963*, 100 – 105.
[38] W. C. Bailey, *Chem. Phys.* **2000**, *252*, 57 – 66.
[39] M. Goubet, R. A. Motiyenko, L. Margulès, J.-C. Guillemin, *J. Phys. Chem. A* **2012**, *116*, 5405 – 5409.
[40] A. C. Legon, *Angew. Chem. Int. Ed.* **1999**, *38*, 2686 – 2714; *Angew. Chem.* **1999**, *111*, 2850 – 2880.
[41] A. P. Cox, S. Waring, K. Morgenstern, *Nat. Phys. Sci.* **1971**, *229*, 22 – 23.
[42] J.-U. Grabow in *Handbook of High-Resolution Spectroscopy, Vol. 2* (Eds.: M. Quack, F. Merkt), Wiley, Chichester, **2011**.
[43] G. Myszkiewicz, W. L. Meerts, C. Ratzer, M. Schmitt, *Phys. Chem. Chem. Phys.* **1968**, *23a*, 68 – 76.
[44] J. A. Ruiz-Santoyo, J. Wilke, M. Wilke, J. T. Yi, D. W. Pratt, M. Schmitt, L. Alvarez-Valtierra, *J. Chem. Phys.* **2016**, *144*, 044303.
[45] Z. Kisiel, E. Bialkowska-Jaworska, L. Pszczolkowski, H. Mäder, J. T. Hougen, *J. Mol. Spectrosc.* **2004**, *227*, 109 – 113.
[46] J. Grabow, W. Stahl, H. Dreizler, *Rev. Sci. Instrum.* **1996**, *67*, 4072 – 4084.
[47] H. D. Rudolph, A. Trinkaus, *Z. Naturforsch.* **2001**, *56*, 635 – 640.
[48] K. Okuyama, N. Mikami, M. Ito, *Laser Chem.* **1987**, *7*, 197 – 211.
[49] C. Thomsen, H. Dreizler, *Z. Naturforsch.* **2001**, *56*, 635 – 640.
[50] A. Jabry, *Spectroscopie à haute résolution de molécules organiques d'intérêt astrophysique et atmosphérique contenant un ou deux rotateurs internes*, Ph.D. of the Sorbonne Paris Cité university, **2016**, p. 231.
[51] I. Kleiner, J. T. Hougen, J. U. Grabow, S. P. Belov, M. Y. Tretyakov, J. Cosléou, *J. Mol. Spectrosc.* **1996**, *179*, 41 – 60.
[52] T. J. Balle, W. H. Flygare, *Rev. Sci. Instrum.* **1981**, *52*, 33 – 45.
[53] S. Kassi, D. Petitprez, G. Wlodarczak, *J. Mol. Spectrosc.* **2004**, *228*, 293 – 297.
[54] Gaussian 09 (Revision D.01), M. J. Frisch, G. W. Trucks, H. B. Schlegel, G. E. Scuseria, M. A. Robb, J. R. Cheeseman, G. Scalmani, V. Barone, B. Mennucci, G. A. Petersson, H. Nakatsuji, M. Caricato, X. Li, H. P. Hratchian, A. F. Izmaylov, J. Bloino, G. Zheng, J. L. Sonnenberg, M. Hada, M. Ehara, K. Toyota, R. Fukuda, J. Hasegawa, M. Ishida, T. Nakajima, Y. Honda, O. Kitao, H. Nakai, T. Vreven, J. A. Montgomery, Jr., J. E. Peralta, F. Ogliaro, M. Bearpark, J. J. Heyd, E. Brothers, K. N. Kudin, V. N. Staroverov, R. Kobayashi, J. Normand, K. Raghavachari, A. Rendell, J. C. Burant, S. S. Iyengar, J. Tomasi, M. Cossi, N. Rega, J. M. Millam, M. Klene, J. E. Knox, J. B. Cross, V. Bakken, C. Adamo, J. Jaramillo, R. Gomperts, R. E. Stratmann, O. Yazyev, A. J. Austin, R. Cammi, C. Pomelli, J. W. Ochterski, R. L. Martin, K. Morokuma, V. G. Zakrzewski, G. A. Voth, P. Salvador, J. J. Dannenberg, S. Dapprich, A. D. Daniels, O. Farkas, J. B. Foresman, J. V. Ortiz, J. Cioslowski, D. J. Fox, Gaussian Inc. Wallingford CT, **2009**.
[55] R. A. Kendall, T. H. Dunning, Jr., R. J. Harrison, *J. Chem. Phys.* **1992**, *96*, 6796 – 6806.
[56] D. E. Woon, T. H. Dunning, Jr., *J. Chem. Phys.* **1994**, *101*, 8877 – 8893.
[57] V. Barone, *J. Chem. Phys.* **2005**, *122*, 014108.
[58] S. Grimme, M. Steinmetz, *Phys. Chem. Chem. Phys.* **2013**, *15*, 16031 – 16042.
[59] M. Goubet, P. Soulard, O. Pirali, P. Asselin, F. Real, S. Gruet, T. R. Huet, P. Roy, R. Georges, *Phys. Chem. Chem. Phys.* **2015**, *17*, 7477 – 7488.
[60] D. R. Herschbach, *J. Chem. Phys.* **1959**, *31*, 91 – 108.

Manuscript received: November 24, 2017
Revised manuscript received: January 12, 2018
Accepted manuscript online: January 12, 2018
Version of record online: February 19, 2018